Received: 3 February 2023 | Revised: 1 September 2023 | Accepted: 8 November 2023

DOI: 10.1002/jrs.6625

RESEARCH ARTICLE

Journal of RAMAN SPECTROSCOPY WILEY

Feasibility of gold nanocones for collocated tip-enhanced Raman spectroscopy and atomic force microscope imaging

Luke R. McCourt[1] | **Ben S. Routley**[1] | **Michael G. Ruppert**[2] | **Andrew J. Fleming**[1]

[1]School of Engineering, University of Newcastle, Callaghan, New South Wales, Australia

[2]School of Mechanical and Mechatronic Engineering, University of Technology Sydney, Ultimo, New South Wales, Australia

Correspondence
Andrew Fleming, School of Engineering, University of Newcastle, Callaghan, NSW 2308, Australia.
Email: andrew.fleming@newcastle.edu.au

Funding information
Australian Research Council Discovery Project, Grant/Award Number: DP210103383

Abstract

Microcantilever probes for tip-enhanced Raman spectroscopy (TERS) have a grainy metal coating that may exhibit multiple plasmon hotspots near the tip apex, which may compromise spatial resolution and introduce imaging artefacts. It is also possible that the optical hotspot may not occur at the mechanical apex, which introduces an offset between TERS and atomic force microscope maps. In this article, a gold nanocone TERS probe is designed and fabricated for 638 nm excitation. The imaging performance is compared to grainy probes by analysing high-resolution TERS cross-sections of single-walled carbon nanotubes. Compared to the tested conventional TERS probes, the nanocone probe exhibited a narrow spot diameter, comparable optical contrast, artefact-free images, and collocation of TERS and atomic force microscope topographic maps. The $1/e^2$ spot diameter was 12.5 nm and 19 nm with 638 nm and 785 nm excitation, respectively. These results were acquired using a single gold nanocone probe to experimentally confirm feasibility. Future work will include automating the fabrication process and statistical analysis of many probes.

KEYWORDS

AFM, collocated, nanocone, plasmon, TERS

1 | INTRODUCTION

Tip-enhanced Raman spectroscopy (TERS) is an imaging technique that allows simultaneous, Raman, and topographical mapping of a surface.[1,2] The optical performance of TERS is dependent on the formation of collective oscillations of surface electrons, known as surface plasmons, on a metal tip.[3,4] Surface plasmons cause charge accumulation at the tip apex, which results in an enhanced electric field that is confined to the surface of the tip.[5] This enhanced electric field is referred to as the near-field and leads to amplified Raman scattering in a small sub-diffraction limited volume.[6,7] The tip-sample separation is controlled using an atomic force microscope (AFM) that gives a topographical estimate of the height of surface features. TERS has been demonstrated to provide sub-diffraction limited chemical mapping of biological samples and surfaces during chemical synthesis.[8–11]

Commercially available TERS probes consist of a silicon AFM probe with a metal coating that forms a rough grain-like structure as illustrated in Figure 1A. The metal coating is typically silver or gold as these materials have

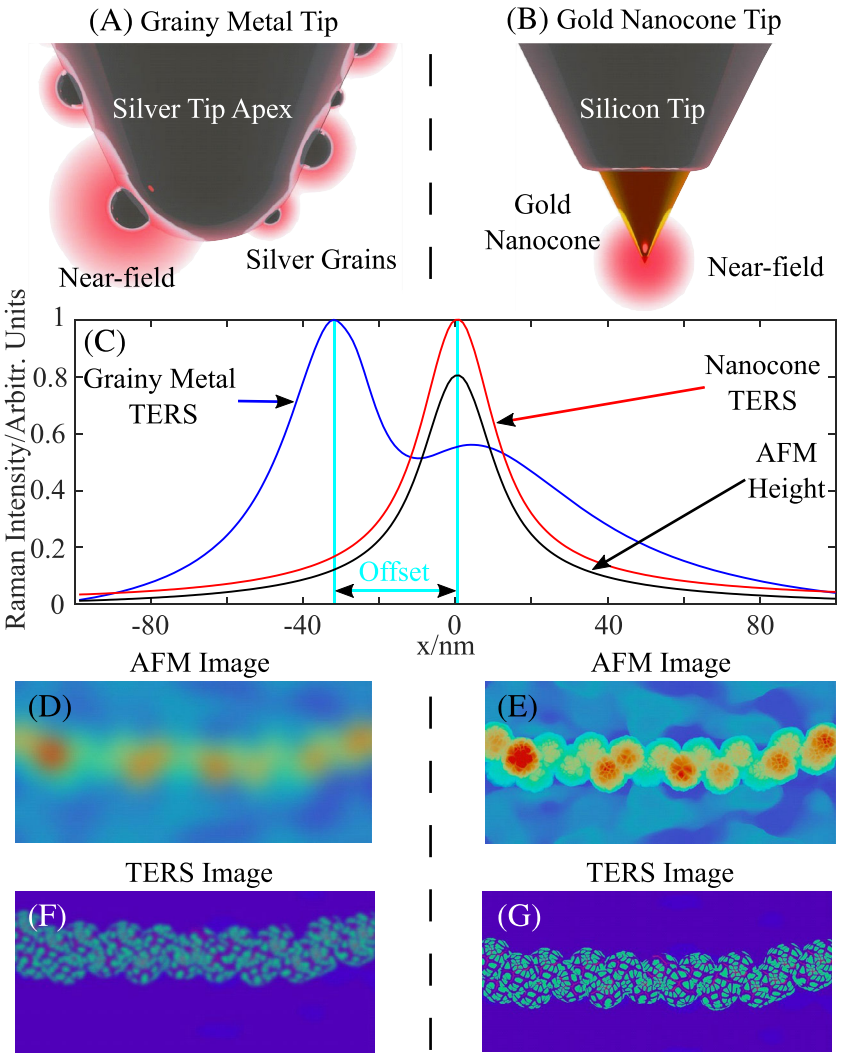

FIGURE 1 An illustrative comparison of a grainy silver probe where a grain has not formed at the tip apex (A) and a gold nanocone probe (B). The electric field distribution under each probe was calculated using boundary element method simulations plotted in (C).[20] The grainy probe has multiple hotspots, resulting in two enhancement peaks that will introduce artefacts into TERS maps. Furthermore, there is an offset between the AFM height and TERS measurements. Finally, the increased tip diameter results in decreased AFM and TERS image resolution shown in (D) and (F), respectively. The nanocone probe circumvents these issues as the physical tip apex functions as a single enhancement site with a small diameter, resulting in artefact-free, high-resolution and collocated AFM and TERS images as shown in (E) and (G).

been shown to offer good electric field enhancement over the visible wavelengths.[12] However, the formation of metal grains and nanoparticles is difficult to control during fabrication.[13] For example, it cannot be guaranteed that a nanoparticle of a certain size will be formed at the mechanical tip apex.[14] This leads to several issues. If a nanoparticle is not present at the tip apex, there may be an offset between the mechanical tip apex and the near-field hotspot, leading to an offset between the TERS and AFM maps as shown in Figure 1C. Furthermore, the presence of more than one nanoparticle at the apex will distort the electric field distribution[15] and create imaging artefacts[16] as shown in Figure 1D,F. The enhancement at the sample will be reduced because the hotspot-sample separation is increased. Finally, the random grain formation causes unreliable performance for grain-based TERS probes. To reduce tip variability, a thick metal coating can be used that increases the likelihood of particle formation at the tip apex. However, this increases the tip radius, which results in decreased AFM and TERS spatial resolution.[17]

Electrochemical etching has been used to produce silver and gold TERS probes with diameters of 50–100 nm.[13] However, this method results in large morphology and enhancement variations from tip to tip.[18] Researchers have estimated that only a few out of 20 manufactured tips will provide adequate near-field enhancement.[19]

A gold nanocone TERS probe is a suitable single-particle TERS probe that circumvents the issues associated with grainy TERS probes as illustrated in Figure 1B. The nanocone approach reduces the potential offset between AFM and TERS images by ensuring the mechanical tip apex and the near-field are collocated as shown in Figure 1C. As there is no requirement for random formation, nanocone probes are expected to be more consistent than metal-coated probes. Control of the nanocone geometry will enable dimension optimisation to maximise enhancement for a given application.[17] A nanocone can be sharpened to a smaller apex diameter than an AFM tip with a thick metal layer and is expected to enable higher resolution AFM and TERS images[21,22] as

shown in Figure 1G. Furthermore, silver nanoparticles corrode in ambient conditions, decreasing plasmon performance.[23] The gold nanocone probes would offer superior lifetimes compared to commercially available silver TERS probes.

The use of nanocone arrays in surface-enhanced Raman spectroscopy is well documented in the literature. The transverse mode of a gold nanocone array has been used to enhance in-plane excitation.[24] Likewise, silicon or silver double nanocone substrates have been shown to improve Raman sensitivity.[25,26] Arrays of gold nanocones have also been fabricated, and the plasmon resonance wavelength has been demonstrated to be tuneable from 600 to 700 nm.[27]

Gold nanocones TERS probes have been successfully fabricated at the tips of AFM probes with lengths ranging from 15 to 175 nm.[21,28] These probes were demonstrated to produce point Raman enhancement and were successfully used for high-resolution topographical measurements as AFM probes. However, in these works, the probes were not demonstrated for TERS imaging, and their performance was not measured or compared to other TERS probes.

The work in this article describes the fabrication of a gold nanocone TERS probe with geometry optimised for 638 nm excitation. The TERS imaging performance of this probe is compared to grainy metal probes. Finally, high-resolution TERS maps acquired using the gold nanocone probe are presented.

2 | METHODS

2.1 | Mathematical model

We have previously modelled gold nanocones using the boundary element method.[17] Empirical models were developed to estimate the dimensions required to tune the fundamental localised surface plasmon resonance to a given wavelength using

$$L = \frac{\lambda_r - 610 + 7.1\theta - 0.3r + \lambda_t}{1.5}, \quad (1)$$

where L is the length (in nm), θ is the cone half angle (in degrees), λ_r is the target resonance wavelength (in nm), r is the tip radius (in nm), and λ_t is the termination constant (in nm). The termination constant λ_t accounts for the shift in resonance wavelength due to the termination on a non-vacuum material. Optical modelling showed a termination offset of +15nm with gold nanocones on silicon and this value is used here. For a 638nm target resonance wavelength, a 28° half-angle and 15nm tip radius, the length of an optimal gold nanocone is expected to be 158nm.

2.2 | Nanocone fabrication

Figure 2 illustrates the gold nanocone fabrication process. The cantilevers were mounted on an aluminium wedge so that a horizontal plane FIB cut would result in a plateau normal to the tip axis as illustrated in Figure 2A1,B1. The AFM tips were FIB milled using a Zeiss Crossbeam 540 FIB-SEM with a 30 kV, 300 pA gallium beam such that a flat triangular plateau approximately 1 μm in diameter was created parallel to the mount base as illustrated in Figure 2C1. A SEM image of the plateau is shown in Figure 2C2. The mount was then placed in an AJA ATC-1800-E electron beam evaporator. Twenty nanometres of titanium at 1 Å/s was deposited followed by 300 nm of gold at 2 Å/s. The titanium acts as an adhesion layer for the gold and improves the otherwise poor adhesion of gold to silicon. The gold layer was made thick enough to accommodate the planned nanocone length. The gold coated probe is illustrated in Figure 2D1. The cantilevers were placed into the FIB with the ion beam oriented co-linearly with the desired tip axis. A 30 kV, 50 pA Ga beam was scanned in an annular, single-pass, reducing spiral with an outer diameter of 3 μm and an inner void diameter of 200 nm, for a total dose of 0.5 nC/μm^2. This produced a sharp nanocone that was approximately 300 nm in length. The scanning pattern is illustrated in Figure 2D2. The overall height of the metal tip was monitored using the secondary electron detector while performing a 0.1 μs dwell time milling scan with the same FIB beam over a 30 μm diameter disc area. The milling was terminated once the desired tip length was achieved as illustrated in Figure 2E2. An SEM image of a successfully fabricated gold nanocone probe is shown in Figure 2E2.

2.3 | Experimental setup

A Horiba XploRA Plus confocal Raman microscope was used in combination with an AIST-NT AFM to control the tip scanning. The system includes the spectrometer and filters to process the Raman scattered light. The inbuilt 785 nm laser source was used as well as an external 638 nm fibre coupled laser. Both lasers were aligned with vertical polarisation. The side-illumination configuration was used where the laser is focused onto the tip apex using the side objective lens. A 100× objective with a numerical aperture of 0.7 was used. A laser power of

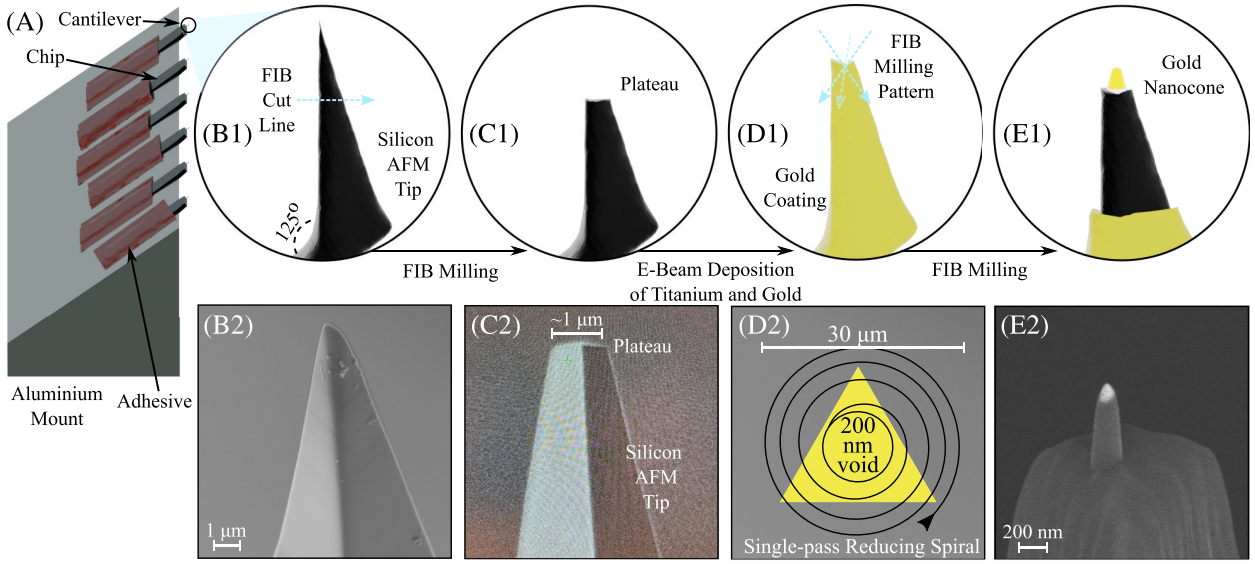

FIGURE 2 Gold nanocone fabrication method and results. The cantilevers were mounted on an aluminium wedge and secured using adhesive tape (A) to achieve a suitable horizontal FIB milling angle. An illustration of the AFM tip with the planned FIB cut line to produce a plateau is shown in (B1). A corresponding SEM image of the tip is shown in (B2). FIB milling is used to create a plateau, which is illustrated in (C1) and a corresponding SEM image is given in (C2). A thin platinum adhesion layer is deposited followed by a thicker gold layer, which is illustrated in (D1). The FIB milling pattern is shown in (D2) and results in a gold nanocone at the tip apex as illustrated in (E1). An SEM image of a 150 nm long gold nanocone TERS probe is shown in (E2).

1 mW measured at the probe was used, resulting in a power density of 2.8×10^5 W/cm^2 and 4.3×10^5 W/cm^2 for the 785 nm and 638 nm laser, respectively. A schematic of the experimental setup is shown in Figure 3A.

2.4 | Quantifying TERS performance

We have previously developed a method for characterising the imaging performance of TERS probes.[29] This involves performing high-resolution cross-section TERS scans of an isolated single-walled carbon nanotube (SWCNT) that acts as a 1D scattering object. The radial breathing mode (RBM) of SWCNTs reveals information about the diameter and local distribution of nanotubes.[30] The diameter of a SWCNT is proportional to the wavenumber of the RBM spectral peak, usually located around 280 cm^{-1} for diameters less than 1 nm. Furthermore, if multiple SWCNTs are bundled together, the RBM will be broadened or have multiple spectral peaks. Thus, a single narrow spectral peak around 280 cm^{-1} indicates an isolated SWCNT that is suitable for use as a 1D scattering object. A high-resolution TERS cross-section of an isolated SWCNT allows calculation of the point spread function (PSF) and hence spot diameter and optical contrast. This method is adopted here and is described in the following.

The sample consisted of dispersed SWCNTs on a gold substrate. An analysis of the spectral RBM peaks of multiple SWCNTs gave an average diameter of 0.85 nm with a standard deviation of 0.01 nm. Tapping mode AFM maps were used to find a suitable sample area consisting of dispersed nanotubes to limit the far-field contribution from multiple nanotubes. The RBM was excited using 785 nm illumination with the tip in contact with the SWCNT as shown in Figure 3C. If the RBM spectral peak was not present, was broadened, or had multiple peaks, the nanotube was assumed to be a bundle and deemed unsuitable.

With the probe in contact with the SWCNT, the Raman acquisition time was minimised while maintaining an acceptably low noise in the point spectrum shown in Figure 3C,D. This reduced the time taken to complete a scan and minimised the impact of slow optical drift. The Raman signal acquired when the tip is in contact with the SWCNT and wile retracted scales linearly with time. Hence the optical contrast is independent of pixel acquisition time. However, a lower acquisition time results in lower total Raman counts and increased noise, which is viewed as an acceptable trade-off. Once a suitable SWCNT is identified, TERS and AFM maps with a resolution of 5×400 are collected simultaneously over an area of 5 nm $\times$ 400 nm. The scanning protocol used was a hybrid mode where the topography measurements are

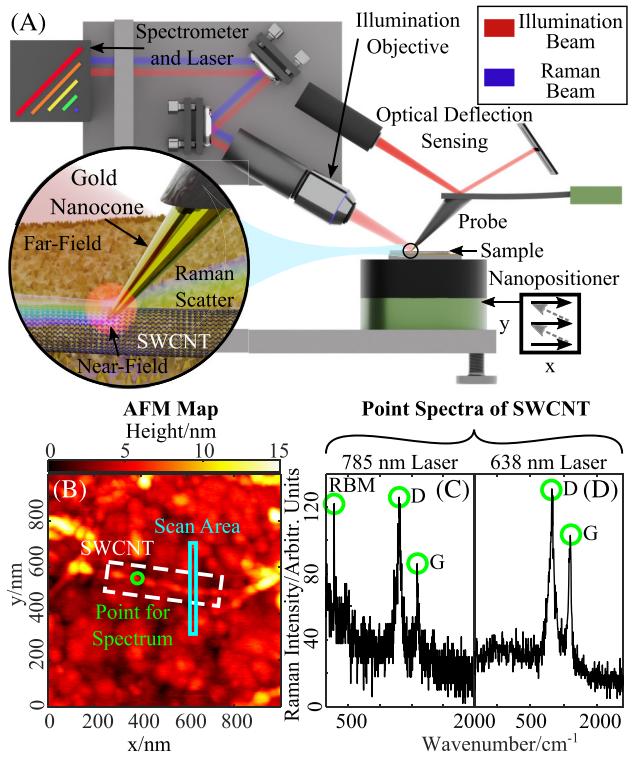

FIGURE 3 (A) Schematic of the experimental setup used for TERS imaging. The microscope is a Horiba XPlora Plus in the side illumination configuration. The inset shows an illustration of a gold nanocone in contact with a SWCNT causing amplification of the Raman scattered light within the near-field volume. (B) An AFM of a suitable area for collecting TERS cross-sections (white box). An example scan area is labelled. (C, D) Example point spectra. The RBM at wavenumber 282.2 cm^{-1} identifies the nanotube as a SWCNT.

acquired using tapping mode AFM, and the Raman measurements are acquired in contact mode AFM for the specified acquisition time. Each SWCNT was used for only a single TERS map to avoid the possibility of photobleaching. Maps were collected at 638 nm and 785 nm using a far-field beam power of 1 mW.

The raw high-resolution TERS SWCNT cross-sections are used to calculate the PSF, optical contrast and spot diameter as follows. Let the Raman map at a given wavenumber be given by

$$M_\omega = \begin{bmatrix} m_{1,1} & \dots & m_{1,400} \\ \vdots & \ddots & \vdots \\ m_{5,1} & \dots & m_{5,400} \end{bmatrix}, \tag{2}$$

where $m_{i,j}$ is the Raman count at a pixel. The rows were aligned so that the SWCNT was positioned at index 200. Assuming a PSF that is symmetric in the x and y-axes:

$$\mathrm{PSF}_{\omega,j} = \frac{\sum_{i=1}^{5} m_{i,j}}{\max\left(\sum_{i=1}^{5} m_{i,j}\right)}. \tag{3}$$

The far-field contribution to the PSF is estimated by taking the average of the PSF with the near-field peak removed:

$$\overline{\mathrm{PSF}}_{\mathrm{ff}} = \frac{\sum_{j=1}^{l} \mathrm{PSF}_{\omega j} + \sum_{j=r}^{end} \mathrm{PSF}_{\omega j}}{n}, \tag{4}$$

where l and r are the j indices two full width half maximums to the left and right of the PSF peak and n is the total number of elements in the numerator.

The near-field PSF is

$$\mathrm{PSF}_{\mathrm{nf}} = \mathrm{PSF} - \overline{\mathrm{PSF}}_{\mathrm{ff}}. \tag{5}$$

The optical contrast is

$$C_\omega = \frac{1 - \overline{\mathrm{PSF}}_{\mathrm{ff}}}{\overline{\mathrm{PSF}}_{\mathrm{ff}}}. \tag{6}$$

The contrast quantifies the ratio of the near-field to far-field contributions. A high contrast allows objects to be distinguished from the substrate. The initial wavenumbers used to calculate the contrast were 285 cm^{-1}, 1292 cm^{-1} and 1606 cm^{-1} for the RBM, D-band and G-band. The wavenumbers that maximised the contrast for each band were selected for final contrast and PSF calculations. The mean contrast was calculated using multiple spectral peaks to minimise the effects of band ratio variations between nanotubes as follows:

$$\overline{C}_{785} = \frac{C_{\mathrm{RBM}} + C_{\mathrm{D}} + C_{\mathrm{G}}}{3} \tag{7}$$

and

$$\overline{C}_{638} = \frac{C_{\mathrm{D}} + C_{\mathrm{G}}}{2}. \tag{8}$$

The spot diameter d is calculated as the diameter where $\mathrm{PSF}_{\mathrm{nf}}$ (Equation 5) falls to $1/e^2$ of the maximum value. The spot diameter is used in this work as a metric for optical resolution. This method was repeated with 638 nm and 785 nm laser excitation using a gold nanocone TERS probe. The results from three commercially available probes previously reported are reproduced in this article for the sake of comparison.[29] The commercially available TERS probes are labelled as follows:

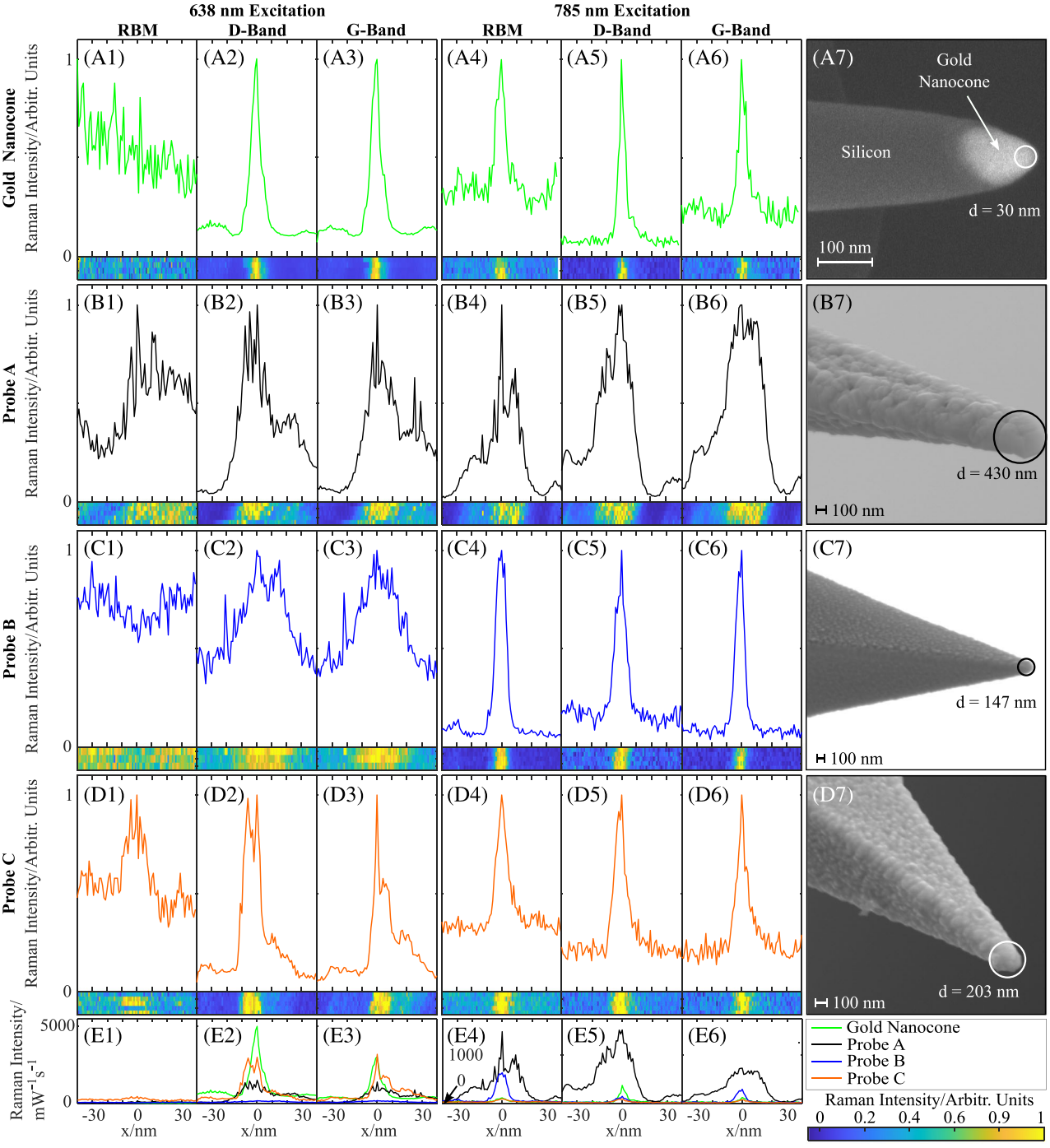

FIGURE 4 Data acquired from high-resolution cross-section TERS maps of SWCNTs. All plots are raw normalised data with no background correction. The RBM, D-band and G-band PSFs for the gold nanocone TERS probe are plotted in (A1–A3) for 638 nm illumination and (A4–A6) for 785 nm excitation. A SEM image of the nanocone is shown in (A7). The results of three commercially available probes are included for comparison.[29] The SWCNT cross-sections with Raman intensity/$mW^{-1}\,s^{-1}$ are plotted in (E1–E6). The PSFs are used to calculate the contrast and spot diameter of each TERS probe, which are summarised in Table 1. The gold nanocone probe fabricated in this work provides the narrowest spot diameter while maintaining adequate contrast at both excitation wavelengths. The probe diameters are estimates taken from the SEM images.

- A - silver coated silicon with a thin gold passivation layer of unknown thickness
- B1, B2 - gold coated silicon
- C1, C2 - gold coated silicon

Probes A and B are both specified by the manufacturer as suitable for use with the TERS setup used in this paper; however, the optimal excitation wavelength is not given. Probe C is not specified as a TERS

TABLE 1 Performance characteristics of TERS probes for imaging SWCNTs at 638 nm and 785 nm laser excitation. The quoted uncertainty is the standard deviation.

Probes	Wavelength (nm)	Contrast D	Contrast G	Contrast RBM	Contrast Mean	Spot Diameter (nm)
Gold Nanocone	638	8.3 ± 0.8	7.3 ± 1.1	N/A	8.1 ± 0.7	19 ± 1
(150nm)	785	10.1 ± 2.5	3.1 ± 0.7	1.8 ± 0.8	6.6 ± 1.3	13 ± 1
A	638	13.6 ± 4.2	9.8 ± 1.1	N/A	11.2 ± 3.3	57 ± 15
	785	44.1 ± 3.6	21.1 ± 6.5	24.6 ± 5.4	33.7 ± 3.7	52 ± 7
B-1	638	1.1 ± 0.4	1.4 ± 0.5	N/A	1.3 ± 0.3	45 ± 17
B-2	785	3.6 ± 0.7	7.2 ± 2.2	13.7 ± 1.5	8.2 ± 1.2	16 ± 2
C-1	638	9.5 ± 2.0	7.7 ± 4.1	1.1 ± 0.5	8.6 ± 2.3	28 ± 7
C-2	785	3.8 ± 0.6	3.7 ± 0.7	2.0 ± 0.2	3.7 ± 0.5	20 ± 2

probe but was selected as it exhibits the characteristics of many gold TERS probes with a grainy gold coating and the correct geometry for side illumination. For the gold nanocone and probe A, TERS cross-sections were acquired using a single probe each. For probes B and C, two probes each were required (one at 638 nm and one at 785 nm) as probe degradation occurred while searching for suitable SWCNTs. The degradation was likely due to a combination of wear and contamination from the sample as several AFM scans were often required to locate a suitable SWCNT. A 0.5 s pixel acquisition time was used for the gold nanocone, probe A and probe B. A 0.1 s pixel acquisition time was used for probe C as this provided sufficient signal-to-noise ratio and longer times did not improve the contrast metric.

3 | RESULTS

3.1 | Far-field and substrate raman spectra

Negligible far-field contribution is observed when the gold nanocone tip, excited at 785 nm, is a short distance from the SWCNT. This is shown in Figure S1 (Supporting Information) by comparing spectra of the probe in contact with an isolated SWCNT and in contact with the gold substrate away from a SWCNT. Additionally, Figure S2 (Supporting Information) shows example Raman spectra with the gold nanocone in contact with an isolated SWCNT on a gold substrate and when retracted. There is negligible far-field due the sparse distribution of nanotubes. These spectra demonstrate the near-field enhancement of the gold nanocone probe.

3.2 | TERS cross-section analysis

Figure 4 shows the measured PSFs of the fabricated gold nanocone probe along with those measured for three commercial probes. The calculated performance metrics are given in Table 1. Details on the experimental protocols are provided in the Supporting Information.

3.2.1 | 638 nm illumination

The PSFs of the gold nanocone probe with 638 nm illumination are shown in Figure 4A1–A3 for the RBM, D-band and G-band, respectively. The D-band and G-band PSFs display a single narrow peak. This is due to a single hot-spot and will allow the nanocone probe to produce artefact-free TERS maps. The calculated spot diameter of 19 nm is significantly narrower than comparable commercial probes where the narrowest spot diameter of 28 nm was achieved using probe C. This suggests that the nanocone probe will produce higher resolution TERS maps.

The gold nanocone achieved an 8.05 mean contrast with 638 nm illumination. This is 28% lower than probe A, 6% lower than probe C, and 650% that of probe B. Hence, the contrast achievable with the gold nanocones is comparable to commercial probes.

The TERS counts for the nanocone probe with 638 nm excitation are given in Figure 4E1–E3 for the RBM, D-band and G-band. The nanocone provides the highest D-band counts indicating that a high total Raman signal is acquired using this probe.

3.2.2 | 785 nm illumination

The PSFs of the gold nanocone probe with 785 nm illumination are shown in Figure 4A4–A6 for the RBM,

D-band and G-band, respectively. The PSFs for the RBM, D-band and G-band all display a single peak. This supports the previous conclusion that this probe has a single hotspot. The calculated spot diameter of 12.5 nm is significantly smaller than the other probes tested.

The gold nanocone achieved a 6.59 mean contrast with 785 nm illumination. This is comparable to the contrast measured with probes C and D but only 20% of probe A. This is thought to be because the 150 nm long nanocone is too short to adequately excite the fundamental plasmon mode at this wavelength.[17] It is expected that a nanocone of optimal length would provide improved contrast.

The TERS counts for the nanocone probe with 785 nm excitation are given in Figure 4E4–E5 for the RBM, D-band and G-band. The nanocone provides lower counts than most of the other probes. This is expected as the geometry was optimised for 638 nm.

3.3 | TERS imaging

Figure 5A1,A2 shows TERS and AFM images of CNT bundles on a gold substrate collected using probe A and 638 nm excitation. This probe features a grainy surface as shown in Figure 4B7. Features are identified and labelled on the TERS map. The TERS D-band counts and AFM height are plotted in Figure 5A3,A4 as a function of distance along the x-profile and y-profile, respectively. There appears to be a minor offset between the TERS and height maps in the x-axis with the maximum of feature

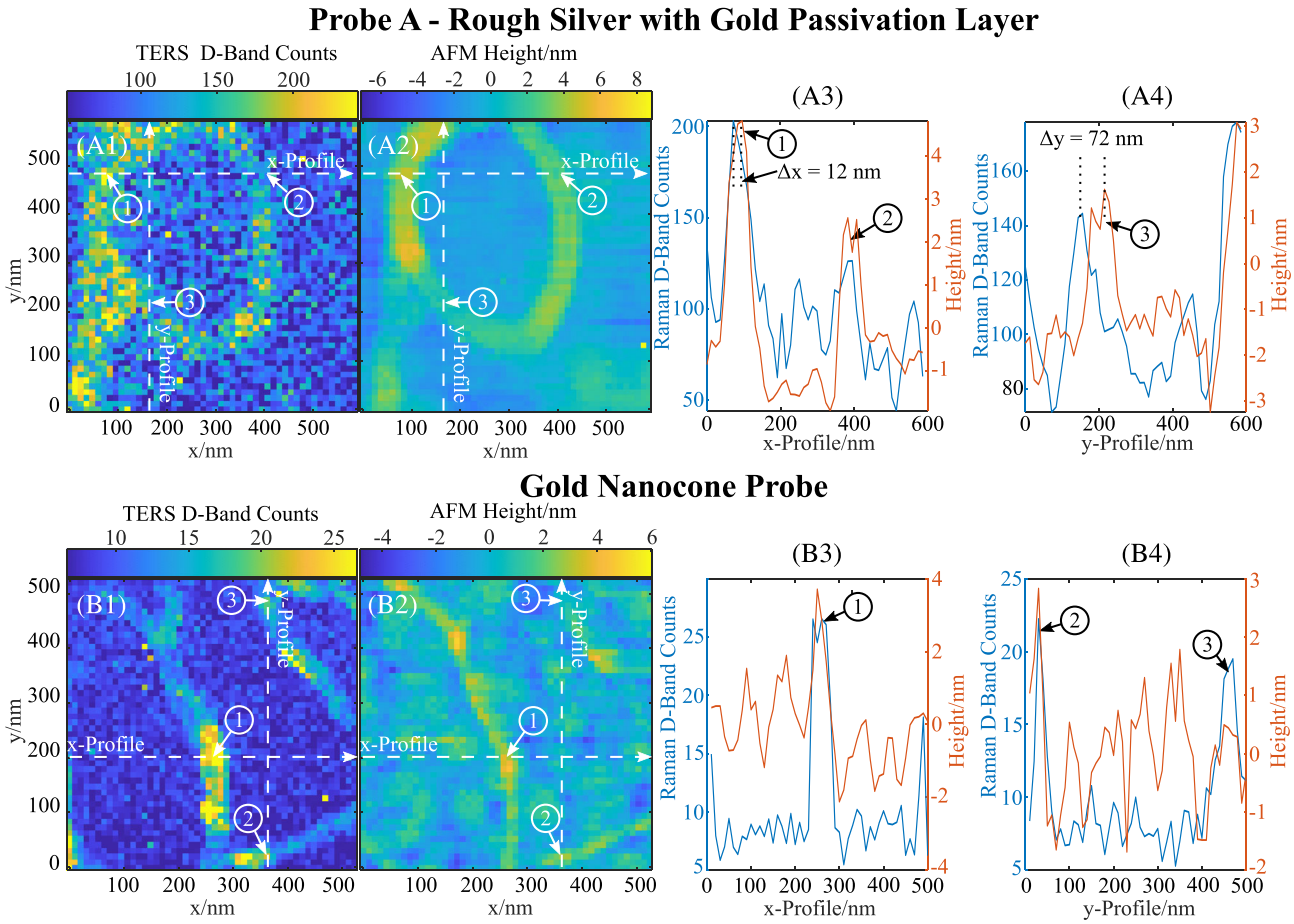

FIGURE 5 Comparison of TERS mapping using probe A and the gold nanocone TERS probe fabricated in this work with 638 nm excitation. The TERS maps are presented with the background spectra removed for each pixel using the ALPS algorithm.[31] The sample consists of CNT bundles on a gold substrate. (A1, B1) D-band TERS maps with features labelled 1–3. (A2, B2) AFM height maps. (A3, B3) Raman D-band counts and AFM height along the x-profile. (A4, B4) Raman D-band counts and AFM height along the y-profile. For probe A, there appears to be an approximately 12 nm offset between the TERS and height maps in the x-axis. Meanwhile, there appears to be a 72 nm offset between the TERS and height maps in the y-axis. The poor collocation seen here is typical of TERS probes with grainy surfaces. The gold nanocone probe exhibits collocation between all labelled features.

1 appearing in the TERS map 12 nm before appearing in the height map. The offset is more significant in the y-axis with the maximum of feature 3 appearing 72 nm earlier in the TERS map compared to the height map. This offset often makes the identification of structures difficult as the AFM height and TERS maps have a spatial offset. The spatial offset becomes significant when small scan areas are used. For example, if a 100 nm × 100 nm scan area is used, then most features appearing on the TERS map will be missing in the topography map and vice versa.

In addition to the cross-sections of SWCNTs, large area TERS maps of carbon nanotube bundles were collected using a nanocone probe and a second example of probe A. This approach allows a direct comparison between the collocation of the AFM and TERS maps. A Horiba TERS test sample was used for these maps, consisting of CNT bundles and graphite flakes on a gold substrate. The maps were collected using the hybrid contact mode.

Figure 5B1,B2 shows TERS and AFM images of CNT bundles on a gold substrate collected using the nanocone TERS probe. The D-band counts and AFM height as a function of distance along the x-profile and y-profile are plotted in (b3) and (b4), respectively. The AFM and TERS maps are collocated with features appearing at the same position in both axes. This demonstrates collocation of TERS and height maps using the nanocone probe, particularly when performing small-area, high-resolution scans.

3.4 | Stability

The TERS maps presented in this work were acquired 12 days after the gold nanocone TERS probe was fabricated. The probe was stored in ambient conditions, and there did not appear to be a noticeable drop in performance over this time period. Longer term stability analysis of the nanocone probes is subject to current research efforts. Given the chemical stability of gold,[32] the nanocone probes are expected to have a longer lifetime than commercially available silver probes (in the authors' opinion).

The gold nanocone probe was used for a mixture of 28 tapping and hybrid-contact mode AFM scans before the acquisition of the TERS results in Figure 5A1–A6 and Figure 5A1–A4. There was no noticeable degradation of the AFM images or decrease in TERS enhancement during these experiments, which suggests a high mechanical stability with the SWCNT sample under study. Further experiments with many probes and different samples are needed.

The nanocone probe was exposed to operating laser power for over 3 h during the acquisition of results presented in this paper. Thus, under the operating conditions presented, the nanocone probe has sufficient thermal stability. However, further investigation is required to determine the effect of higher laser power.

3.5 | Study limitations

The results presented in this article were acquired using a single gold nanocone probe and a single sample. Equation (1) has not been experimentally verified and it is possible that the 150 nm long nanocone presented here is not optimal for 638 nm excitation. Furthermore, the repeatability of the manufacturing process has not been demonstrated. Many more production runs and imaging experiments are required to determine the statistical variations in the manufacturing process and probe performance. Furthermore, the nanocone probe was compared to a limited set of grainy TERS probes, which are known to exhibit large variations between probes.[13,14] A larger set of grainy probes would permit a statistical analysis of probe performance and a more conclusive comparison with nanocone probes. Future research will focus on automating the nanocone fabrication process to allow higher production rates and a statistical analysis of probe performance.

All results presented in this paper were acquired on gold substrates, which may result in stronger gap modes when combined with a gold TERS probe.[33] This may bias results towards the gold nanocone probe. Future work should investigate the effects of different substrates.

The PSFs, optical contrast and spot diameters were calculated under the assumption that the near-field distribution is symmetric in the sample plane, which may not be true. Future work should investigate potential asymmetries by acquiring the PSF in both dimensions of the sample plane.

4 | CONCLUSION

This article demonstrates the feasibility of using gold nanocone probes for tip-enhanced Raman spectroscopy (TERS). The proposed nanocone probe appears to mitigate some of the limitations encountered with commercial TERS probes, namely, variable spatial TERS resolution, multiple enhancement sites that can introduce imaging artefacts and misaligned TERS and AFM images. The nanocone probe exhibited the narrowest spot diameter of 12.5 nm and 19 nm with 638 nm and 785 nm illumination, respectively. The nanocone also exhibited

comparable contrast to the commercial probes with 638 nm and 785 nm illumination and was free from multiple hotspots. As the single gold nanoparticle forms both the TERS hotspot and mechanical apex, the AFM and TERS maps were advantageously collocated. Finally, the nanocone probe was stored in ambient conditions without noticeable performance degradation over a 2-week period.

Despite the possible performance and practical advantages of gold nanocone probes, the present fabrication complexity makes them uncompetitive against silver coated probes, especially for TERS imaging on flat surfaces where there may be little performance benefits. Current work includes automating the fabrication process to increase the number of probes per batch and reduce the operator time. If this is successful, nanocone probes may offer a viable alternative for applications that require a long probe lifetime, or simultaneous AFM and TERS imaging.

To the knowledge of the author, the work presented here contains the first high-resolution TERS maps acquired with a gold nanocone probe. Future work involves a statistical analysis of many nanocone probes to experimentally determine optimal geometries at different excitation wavelengths.

AUTHOR CONTRIBUTIONS

Luke R. McCourt and Ben S. Routley performed the experiments. Luke R. McCourt analysed the data. Luke R. McCourt, Michael G. Ruppert and Andrew J. Fleming wrote the manuscript. All authors contributed to the discussion of the results.

ACKNOWLEDGEMENTS

The authors would like to acknowledge the Research and Prototype Foundry at The University of Sydney for assisting with the fabrication of the gold nanocone TERS probes. Open access publishing facilitated by The University of Newcastle, as part of the Wiley - The University of Newcastle agreement via the Council of Australian University Librarians.

CONFLICT OF INTEREST STATEMENT

The authors declare no potential conflict of interests.

ORCID

Luke R. McCourt https://orcid.org/0000-0003-0593-6054
Michael G. Ruppert https://orcid.org/0000-0003-2286-4929

REFERENCES

[1] F. Shao, R. Zenobi, *Analyt. Bioanalyt. Chem.* **2019**, *411*(1), 37.
[2] T. Touzalin, S. Joiret, I. T. Lucas, E. Maisonhaute, *Electrochem. Commun.* **2019**, *108*, 106557.
[3] H. Furukawa, S. Kawata, *Opt. Commun.* **1998**, *148*(4), 221.
[4] H. Raether, *in Surface plasmons on smooth and rough surfaces and on gratings*, Springer **1988**, 4.
[5] M. Pelton, G. W. Bryant, *in Introduction to metal-nanoparticle plasmonics*, vol. 5, John Wiley & Sons **2013**, xi.
[6] N. Hayazawa, Y. Inouye, Z. Sekkat, S. Kawata, *Chem. Phys. Lett.* **2001**, *335*(5), 369.
[7] R. M. Stöckle, Y. D. Suh, V. Deckert, R. Zenobi, *Chem. Phys. Lett.* **2000**, *318*(1), 131.
[8] D. Alastair Smith, S. Webster, M. Ayad, S. D. Evans, D. Fogherty, D. Batchelder, *Ultramicroscopy* **1995**, *61*(1), 247.
[9] S. Ambardar, D. V. Voronine, in 2018 IEEE Research and Applications of Photonics In Defense Conference (RAPID) **2018**, 1.
[10] R. Böhme, D. Cialla, M. Richter, P. Rösch, J. Popp, V. Deckert, *J. Biophotonics* **2010**, *3*(7), 455.
[11] T. Schmid, L. Opilik, C. Blum, R. Zenobi, *Angewandte Chemie Int. Ed.* **2013**, *52*(23), 5940.
[12] K. S. Lee, M. A. El-Sayed, *J. Phys. Chem. B* **2006**, *110*(39), 19220.
[13] T.-X. Huang, S.-C. Huang, M.-H. Li, Z.-C. Zeng, X. Wang, B. Ren, *Analyt. Bioanalyt. Chem.* **2015**, *407*(27), 8177.
[14] L. Ramanauskaite, H. Xu, E. Griskonis, D. Batiuskaite, V. Snitka, *Plasmonics* **2018**, *13*(6), 1907.
[15] J. P. Camden, J. A. Dieringer, Y. Wang, D. J. Masiello, L. D. Marks, G. C. Schatz, R. P. Van Duyne, *J. Am. Chem. Soc.* **2008**, *130*(38), 12616.
[16] W. Zhang, Cui, B.-S. Yeo, T. Schmid, C. Hafner, R. Zenobi, *Nano Lett.* **2007**, *7*(5), 1401.
[17] L. R. McCourt, M. G. Ruppert, B. S. Routley, S. C. Indirathankam, A. J. Fleming, *J. Raman Spectrosc.* **2020**, *51*(11), 2208.
[18] (Eds: S. Kawata, V. M. Shalaev), *Tip enhancement Edited by* S. Kawata, V. M. Shalaev, Advances in Nano-Optics and Nano-Photonics, Elsevier, Amsterdam; Boston **2007**.
[19] Y. Fujita, P. Walke, S. De Feyter, H. Uji-i, *Japan. J. Appl. Phys.* **2016**, *55*(8S1), 8NA02.
[20] U. Hohenester, A. Trügler, *Comput. Phys. Commun.* **2012**, *183*(2), 370.
[21] M. Fleischer, A. Weber-Bargioni, M. V. P. Altoe, A. M. Schwartzberg, P. J. Schuck, S. Cabrini, D. P. Kern, *ACS Nano* **2011**, *5*(4), 2570.
[22] L. Zhang, H. Liu, L. Chen, P. Guan, B. Chen, T. Fujita, Y. Yamaguchi, H. Iwasaki, Q.-K. Xue, M. Chen, *RSC Adv.* **2016**, *6*(4), 2882.
[23] V. J. Keast, *Appl. Nanosci.* **2022**, *12*(6), 1859.
[24] Y. S. Hu, J. Jeon, T. J. Seok, S. Lee, J. H. Hafner, R. A. Drezek, H. Choo, *ACS Nano* **2010**, *4*(10), 5721.
[25] L. Mehrvar, M. Sadeghipari, S. H. Tavassoli, S. Mohajerzadeh, M. Fathipour, *Scientif. Rep.* **2017**, *7*(1), 12106.
[26] S. Rao, M. J. Huttunen, J. M. Kontio, J. Makitalo, M.-R. Viljanen, J. Simonen, M. Kauranen, D. Petrov, *Opt. Express* **2010**, *18*(23), 23790.

[27] B. Hoffmann, S. Vassant, X.-W. Chen, S. Götzinger, V. Sandoghdar, S. Christiansen, *Nanotechnology* **2015**, *26*(40), 404001.
[28] O. Tanirah, D. P. Kern, M. Fleischer, *Microelectron. Eng.* **2015**, *141*, 215.
[29] L. R. McCourt, B. S. Routley, M. G. Ruppert, V. J. Keast, C. I. Sathish, R. Borah, R. V. Goreham, A. J. Fleming, *ACS Appl. Nano Mater.* **2022**, *5*(7), 9024.
[30] S. Costa, E. Borowiak-Palen, M. Kruszy, A. Bachmatiuk, R. J. Kale, *Mater. Sci.-Poland* **2008**, *26*(2), 433.
[31] P. J. Cadusch, M. M. Hlaing, S. A. Wade, S. L. McArthur, P. R. Stoddart, *J. Raman Spectrosc.* **2013**, *44*(11), 1587.
[32] D. Cabuzu, A. Cirja, R. Puiu, A. Mihai Grumezescu, *Current Top. Medic. Chem.* **2015**, *15*(16), 1605.
[33] J. Stadler, B. Oswald, T. Schmid, R. Zenobi, *J. Raman Spectrosc.* **2013**, *44*(2), 227.

SUPPORTING INFORMATION

Additional supporting information can be found online in the Supporting Information section at the end of this article.

How to cite this article: L. R. McCourt, B. S. Routley, M. G. Ruppert, A. J. Fleming, *J Raman Spectrosc* **2023**, 1. https://doi.org/10.1002/jrs.6625